IEEE Access
Multidisciplinary | Rapid Review | Open Access Journal

IEEE POWER & ENERGY SOCIETY SECTION

Received 12 December 2023, accepted 7 January 2024, date of publication 10 January 2024, date of current version 24 January 2024.

Digital Object Identifier 10.1109/ACCESS.2024.3352258

RESEARCH ARTICLE

Active High-Impedance Fault Detection Method for Resonant Grounding Distribution Networks

ZHIWEI YAO[1], YANG LIU[1], (Member, IEEE), JIAN CHEN[2], JINPENG JI[1], MENGDI ZHANG[1], AND YANYONG GONG[1]

[1]School of Electrical and Electronic Engineering, Shandong University of Technology, Zibo 255000, China
[2]Zibo Metrology Technology Research Institute, Zibo 255025, China

Corresponding author: Yang Liu (bqxyl@sdut.edu.cn)

This work was supported in part by the State Grid Corporation of China Technology Project 52094017003D.

ABSTRACT Aimed at the high-impedance fault detection problem, this paper proposes a fault-feature enhancement method for actively detecting high-impedance faults. The essential characteristic of this method is that the fault features are actively enhanced without affecting the normal terminal voltage. The method consists of two stages, i.e., the feature-enhancement stage and the fault-detection stage. The terminal voltage difference between the fault and normal state is analyzed in the first stage. Then, the feasibility of enhancing terminal voltage difference by the auxiliary signal is proved, and the selection criteria of the auxiliary signal is determined based on IEEE standards. In the second stage, the local-scale energy entropy ratios are applied to reconstruct the measurements. Then, high-impedance faults are detected by discriminating reconstructed data statistical characteristics differences before and during the fault. The simulation results show that the proposed method can accurately identify high-impedance faults with 75 kΩ transition impedance in an environment with a signal-to-noise ratio of 15 dB and reliably detect the faults with 75 kΩ transition impedance on buses and feeders at different positions. The method is robust to noise, transition impedance, and switching events.

INDEX TERMS Active detection, feature enhancement, high-impedance faults, fault detection, distribution.

ABBREVIATIONS

RG	Resonance Grounding.
HIF	High-Impedance Fault.
SNR	Signal-To-Noise Ratio.
DC	Direct Current.
AC	Alternating Current.
ST	Stockwell Transform.
CGAN	Conditional Generative Adversarial Network.
CNN	Convolutional Neural Network.
TVKF	Time-Varying Kalman Filter.
ITD	Intrinsic Time Decomposition.
WT	Wavelet Transform.
ZSC	Zero-Sequence Current.
MCEEMD	Modified Complete Ensemble Empirical Mode Decomposition.
ALO	Ant Lion Optimizer.
ANN	Artificial Neural Network.
LSTM	Long Short-Term Memory.
DRL	Deep Reinforcement Learning.
MSVM	Multiclass Support Vector Machine.
TL	Transfer Learning.
KLD	Kullback-Leibler Divergence.
JSD	Jensen-Shannon Divergence.
PCA	Principal Component Analysis.
WD	Wasserstein Divergence.
SI	Signal Injection.
VMD	Variational Mode Decomposition.
IMF	Intrinsic Mode Function.
LLS	Linear Load Switching.
NLS	Nonlinear Load Switching.

The associate editor coordinating the review of this manuscript and approving it for publication was Sarasij Das.

CS	Capacitor Switching.
TE	Transformer Energizing.
PVS	Photovoltaic Switching.
AFFE	Active Fault Feature Enhancement.
MM	Mathematical Morphology.
DT	Decision Tree.
SR	Stochastic Resonance.
SWT	Stationary Wavelet Transform.
DFT	Discrete Fourier Transform.
KF	Kalman Filter.

NOMENCLATURE

l	The length of the $k-$th feeder line.
ω	Power grid frequency.
$\boldsymbol{Z_k}$	The line impedance of the $k-$th feeder line.
$\boldsymbol{Y_k}$	The line ground admittance of the $k-$th feeder line.
$\boldsymbol{R_k}, \boldsymbol{L_k}$	The resistance and the inductance of the $k-$th feeder line.
$\boldsymbol{G_k}$,$\boldsymbol{C_k}$	The ground conductivity and ground capacitance of the $k-$th feeder line.
$\boldsymbol{L_z}$	The inductance of the resonant.
$\boldsymbol{U_k^{\mathrm{q}}(s)}$	The terminal voltage of the $k-$th feeder.
$\boldsymbol{U(s)}$	The power supply voltage.
$\boldsymbol{I_k^{\mathrm{p}}(s)}$	The terminal current of the $k-$th feeder.
f, d	The fault point and the distance from the beginning of the line to the fault point.
$\boldsymbol{R_f}$	The transition impedance.
$\widehat{\boldsymbol{Z}}_{\mathrm{k}}(s)$	The equivalent impedance of $k-$th feeder.
$\widehat{\boldsymbol{Y}}_k^{\mathrm{p}}(s)$,$\widehat{\boldsymbol{Y}}_k^{\mathrm{q}}(s)$	The equivalent admittance and the equivalent admittance of the beginning and end of $k-$th feeder.
$\boldsymbol{R}_{\mathrm{eq}}$, $\boldsymbol{L}_{\mathrm{eq}}$	The equivalent resistance and the equivalent inductance of the line of the k-th feeder.
$\boldsymbol{G}_{\mathrm{eq}}^{\mathrm{p}}$, $\boldsymbol{C}_{\mathrm{eq}}^{\mathrm{p}}$	The equivalent conductivity at the beginning and the equivalent capacitance at the beginning of the line of the k-th feeder.
$\boldsymbol{G}_{\mathrm{eq}}^{\mathrm{q}}$, $\boldsymbol{C}_{\mathrm{eq}}^{\mathrm{q}}$	The equivalent conductivity at the end and the equivalent capacitance at the end of the line of the $k-$th feeder,.
$\boldsymbol{\Delta U(s)}$	The terminal voltage difference before and during the fault.
ψ	The adjusting parameter.
Υ	And the auxiliary voltage signal.
$\widetilde{\boldsymbol{U}}_{\boldsymbol{kf}}^{\mathfrak{q}}\boldsymbol{(s)}$	The terminal voltage with auxiliary signals.
$\boldsymbol{u_k}$	The $k-$th IMF.
$\boldsymbol{\delta(t)}$	The decimated dyadic filter bank kernel function.
$\boldsymbol{\omega}_{\mathrm{k}}$	The central frequency corresponding to the $k-$th IMF.
$\widetilde{\boldsymbol{u}}$	The voltage data set decomposed.
$E_k(n)$	The energy sequence of the $k-$th IMF.
$\Re_k(i)$	The energy entropy.
$\kappa_k(n)$	The ratios of the $k-$th IMF energy to the total energy.
ϕ	The window length.
δ_k^i	The weight.
$\overline{\Re}_k(i)$,$\widehat{\Re}_k(i)$	The energy entropy of the $k-$th imfs for the historical and measured data in the $i-$th window.
$\hat{\boldsymbol{u}}_k$	The reconstructed $k-$th IMF.
$\boldsymbol{u_k^i}$	The $k-$th IMF of the measured data in the $i-$th window.
N	The total number of samples.
$\boldsymbol{u}$	The data reconstructed.
$\overline{\boldsymbol{u}}$, $\widehat{\boldsymbol{u}}$	The reconstructed normal data and measured data.
$\overline{\boldsymbol{P}}$, $\widehat{\boldsymbol{P}}$	The probability distributions of $\overline{\boldsymbol{u}}$ and $\widehat{\boldsymbol{u}}$.
$\boldsymbol{\xi}$	The detection threshold.
μ, σ, τ	The mean value of Wasserstein divergence, the standard deviation of Wasserstein's divergence, and the constant.
W_2	The Wasserstein divergence.
t_{d}, t_{w}	The duration of exceeding the limit and the determination time limit.

I. INTRODUCTION

RG distribution networks are adopted in China and most European countries [1], [2]. Because the fault current is very weak when a single-phase-to-ground fault occurs in the RG distribution networks, most of the overcurrent relays do not trip. When the high-impedance fault occurs, this situation is particularly serious due to the large grounding resistance, it is difficult to detect HIF in the system on time. Therefore, high-impedance fault detection has attracted more and more research interest.

Most HIF detection methods use signal processing technologies to extract time-domain, frequency-domain, and time-frequency domain features for voltage and current profiles. For example, in time-domain methods, [3] used the time-domain reflection method to detect high impedance faults. In the frequency domain method, [4] used the cumulative error indicator to monitor the phase angle of the third harmonic and extract it through the Stockwell transform for fault detection and classification. Reference [5] used the third harmonic angle of the current as a practical feature for fault detection. Reference [6] used the harmonic components of voltage and current for each phase and then calculated the reactive power of each phase using the harmonic components

TABLE 1. Comparison of this method with other relevant methods in the literature.

Ref.	Measurement	Detection method	Noise	Field test	Switching event
[3]	Voltage, Current	Pulses	No	No	No
[4]	Current	ST	No	Yes	Yes
[5]	Current	CGAN-CNN	No	No	Yes
[6]	Voltage, Current	TVKF	No	No	No
[7]	Current	ITD	Yes	No	Yes
[8]	Current	WT	No	Yes	Yes
[9]	Current	ZSC	No	Yes	No
[11]	Current	MCEEMD	Yes	No	Yes
[12]	Voltage, Current	ALO-ANN	No	No	No
[13]	Current	LSTM	No	No	Yes
[14]	Voltage, Current	CNN-DRL	No	No	No
[15]	Voltage, Current	MSVM	No	No	Yes
[16]	Voltage, Current	TL	Yes	Yes	Yes
[18]	Current	KLD	No	No	Yes
[19]	Current	JSD-PCA	Yes	No	Yes
[21]	Current	WD	Yes	Yes	Yes
[22]	Current	SI	No	No	No
[23]	Current	SI	Yes	No	No
[24]	Voltage	SI	No	No	No
[25]	Voltage	SI	No	No	No

for fault detection. In the time-frequency domain method. Reference [7] proposed a HIF detection method based on intrinsic time decomposition and the Teager Kaiser energy operator. Reference [8] used discrete wavelet transform to extract detailed energy content features of coefficients from the extracted current signal for fault detection. Reference [9] used a wavelet pack algorithm to analyze the characteristics of zero sequences' current variation in feeder lines. Then, fault detection criteria are constructed using spectral energy and zero sequence current direction. Reference [10] analyzed and evaluated arc faults' transient and steady-state dynamic states through time-frequency domain analysis. Reference [11] used an improved adaptive noise fully integrated empirical mode decomposition method to extract the second intrinsic mode function and calculate its Teager Kaiser energy operator to achieve HIF detection. Besides, machine learning-based methods, [12] used a combination of ant lion optimizer and artificial neural network to accurately separate HIF. Reference [13] classified the energy characteristics of current using a short-term and short-term memory network of a recurrent neural network for fault detection. Reference [14] utilized a hybrid model of convolutional neural networks and deep reinforcement learning to identify and locate faults in transmission lines. In multivariate statistical methods, [15] used multiple algorithms such as principal component analysis, Fisher discriminant analysis, and binary and multi-class support vector machines to detect and identify high-impedance faults. Reference [16] integrated all features from different distribution networks to form a basic cloud convolutional neural network model for HIF detection. Reference [17] used dual-channel convolutional neural networks for high-impedance fault detection. In the statistical divergence method, [18] used the Kullback Leibler divergence similarity measure to quantify the nonlinear and asymmetric features of the subsequent two half cycles of the current waveform into HIF detection criteria for HIF detection. Reference [19] detected HIF through multivariate Jensen-Shannon divergence similarity measurement. Reference [20] adopts an intelligent fault diagnosis method based on Wasserstein gradient penalty generation adversarial networks using deep autoencoders. Reference [21] used sparse principal component analysis to extract joint features from measurement data and Wasserstein divergence to detect HIF. The above method is applied to detect HIF in medium voltage networks. Despite good detection performance, most methods implicitly assume that faults may be known to occur, which means that such methods are passive in detecting faults, active fault detection can better highlight fault characteristics and further improve the reliability and safety of passive fault detection. Therefore, how to actively detect high-impedance faults without knowing whether the fault occurs has become a challenging problem.

The method of actively detecting faults by injecting auxiliary signals into the line to enhance fault characteristics has received continuous attention, Song et al. [22] proposed the fault localization and isolation method based on the current distribution characteristics of the injected signals based on the preliminary discrimination of the fault. Reference [23] made a preliminary judgment on whether a fault occurs and then applied a controllable modular multilevel converter to inject sinusoidal signals for fault detection, similar to [22]. Similarly, [24] proposed a fault localization method based on an active pulse modular multilevel converter. This method generates traveling wave pulses propagating to the line by controlling sub-modules in a modular multilevel converter. Reference [25] was based on the collected active pulses after fault occurrence as features and employed support vector machines to detect faults. However, most active detection methods inject auxiliary signals online to determine whether a fault has occurred, which is based on the preliminary judgment on whether the fault has occurred. Furthermore, these methods are all aimed at DC distribution networks. The large-scale access to DGs makes it possible to inject auxiliary signals online into the AC distribution grid. Therefore, how to actively detect high-resistance faults by injecting auxiliary signals online into the lines without affecting the regular operation of the AC distribution network has become a challenging and fascinating problem.

Therefore, this paper proposes an active high-impedance fault detection method using injected auxiliary signals in the AC distribution grid. Based on the difference in voltage signals between pre-fault and post-fault terminals, the method reconstructs the power frequency voltage signal using the local-scale energy entropy ratio. The statistical feature differences in voltage before and during the fault process are utilized to achieve high-impedance fault detection and identification. To test the effectiveness, simulations and tests are carried out under various scenarios. The literature review comparison is as follows.

The contributions of this paper is summarized as follows.

1) This paper proposed AFFE, which can eliminate the impact of auxiliary signals on the system under normal operating conditions. The actively injected auxiliary signals only enhance the fault characteristics during the fault period. AFFE can make fault detection methods more sensitive.
2) Use the local energy entropy method to reconstruct data to highlight fault features, and use Wasserstein divergence for fault detection. This method improves the tolerance for uncertain factors such as fault environment and fault medium conditions.
3) Distinguishing transient events between HIF and distribution networks, and ensuring that protection does not malfunction.

The remainder of the paper is organized as follows. Section II mainly analyzes the principle of fault feature enhancement in RG distribution networks and the reconstruction of enhanced voltage signals. In Section III mainly discusses the basis for selecting the amplitude and frequency of auxiliary signals. In Section IV, PSCAD was used to conduct a series of studies on different fault scenarios and switching events to verify the feasibility and effectiveness of the proposed active enhancement method. The Section V uses on-site experimental data to further validate the proposed method. Finally, draw a conclusion in Section VI.

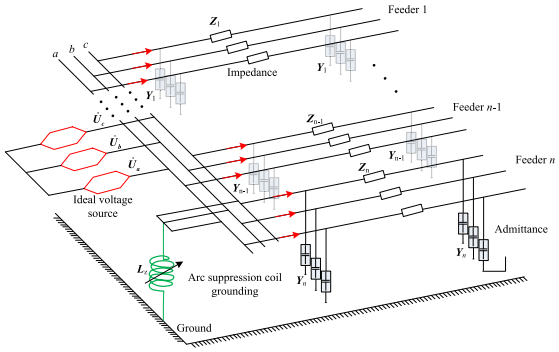

FIGURE 1. Normal equivalent circuit.

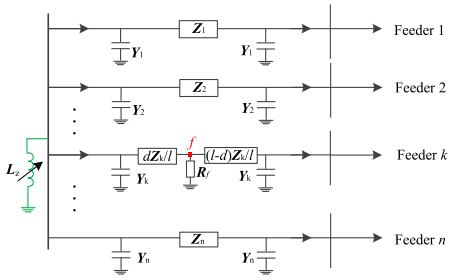

FIGURE 2. Fault equivalent circuit.

II. ACTIVE HIF DETECTION METHOD

A. ACTIVE FAULT-FEATURE ENHANCEMENT

Consider the normal operation of the power system, the equivalent circuit of the system with resonant grounding is shown in Figure 1.

As shown in Figure 1, the system grounded through resonant has n feeders. According to the Laplace transform principle, the terminal voltage of the $k-$th feeder is

$$\boldsymbol{U}_k^{\mathrm{q}}(s) = \boldsymbol{A}\boldsymbol{B}\boldsymbol{U}(s) - \boldsymbol{D}\boldsymbol{I}_k^{\mathrm{p}}(s) \tag{1}$$

where $\boldsymbol{A} = 1/\boldsymbol{G}_k + (\boldsymbol{R}_k + s\boldsymbol{L}_k)[1 + s\boldsymbol{C}_k/\boldsymbol{G}_k + 1/(s\boldsymbol{L}_z\boldsymbol{G}_k)]$, $\boldsymbol{B} = \boldsymbol{G}_k$, $\boldsymbol{D} = \boldsymbol{R}_k + s\boldsymbol{L}_k$.

If a single-phase grounding high-impedance fault occurs on the $k-$th feeder, the equivalent circuit of the line fault is shown in Figure 2.

Furthermore, the circuit of the k-th feeder, as shown in Figure 2, can be transformed to the following form, as illustrated in Figure 3.

According to the Laplace transform, the parameters, as shown in Figure 3, are obtained as follows

$$\widehat{\boldsymbol{Z}}_k(s) = \boldsymbol{R}_{\mathrm{eq}} + s\boldsymbol{L}_{\mathrm{eq}}$$

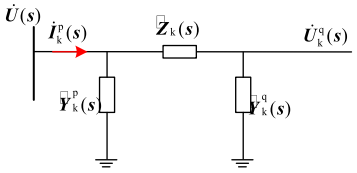

FIGURE 3. Equivalent π type circuit.

$$\begin{aligned}\widehat{\boldsymbol{Y}}_k^{\mathrm{p}}(s) &= \boldsymbol{G}_{\mathrm{eq}}^{\mathrm{p}} + s\boldsymbol{C}_{\mathrm{eq}}^{\mathrm{p}} + \frac{1}{s\boldsymbol{L}_{\mathrm{z}}}\\ \widehat{\boldsymbol{Y}}_k^{\mathrm{q}}(s) &= \boldsymbol{G}_{\mathrm{eq}}^{\mathrm{q}} + s\boldsymbol{C}_{\mathrm{eq}}^{\mathrm{q}}\end{aligned} \tag{2}$$

the equivalent parameters are obtained as the following form

$$\begin{aligned}\boldsymbol{R}_{\mathrm{eq}} &= d\,(l - d)\left(\boldsymbol{R}_k{}^2 - \omega^2\boldsymbol{L}_k{}^2\right)/\left(l^2\boldsymbol{R}_f\right) + \boldsymbol{R}_k\\ \boldsymbol{L}_{\mathrm{eq}} &= 2d\,(l - d)\,\boldsymbol{R}_k\boldsymbol{L}_k/\left(l^2\boldsymbol{R}_f\right) + \boldsymbol{L}_k\\ \boldsymbol{G}_{\mathrm{eq}}^{\mathrm{p}} &= (l - d)\left[(l - d)\,d\boldsymbol{R}_k/l^2 + \boldsymbol{R}_f\right]/\left(l\boldsymbol{M}^2 + l\boldsymbol{N}^2\right) + \boldsymbol{G}_k\\ \boldsymbol{C}_{\mathrm{eq}}^{\mathrm{p}} &= -(l - d)^2 d\boldsymbol{L}_k/\left(l^2\boldsymbol{M}^2 + l^2\boldsymbol{N}^2\right) + C_k\\ \boldsymbol{G}_{\mathrm{eq}}^{\mathrm{q}} &= d\left[(l - d)\,d\boldsymbol{R}_k/l^2 + \boldsymbol{R}_f\right]/\left(l\boldsymbol{M}^2 + l\boldsymbol{N}^2\right) + \boldsymbol{G}_k\\ \boldsymbol{C}_{\mathrm{eq}}^{\mathrm{q}} &= -(l - d)\,d^2\boldsymbol{L}_k/\left(l^2\boldsymbol{M}^2 + l^2\boldsymbol{N}^2\right) + C_k\end{aligned} \tag{3}$$

where $\boldsymbol{M} = d\,(l-d)\,\boldsymbol{R}_k/l^2 + \boldsymbol{R}_f$ and $\boldsymbol{N} = \omega d\,(l-d)\,\boldsymbol{L}_k/l^2$.

Therefore, the terminal voltage of the line during the fault is

$$\boldsymbol{U}_{kf}^{\mathrm{q}}(s) = \boldsymbol{A}_f\boldsymbol{B}_f\boldsymbol{U}(s) - \boldsymbol{D}_f\boldsymbol{I}_k^{\mathrm{p}}(s) \tag{4}$$

where $\boldsymbol{A}_f$, $\boldsymbol{B}_f$, and $\boldsymbol{D}_f$ are obtained as $\boldsymbol{A}_f = 1/\boldsymbol{G}_{\mathrm{eq}}^{\mathrm{p}} + (\boldsymbol{R}_{\mathrm{eq}} + s\boldsymbol{L}_{\mathrm{eq}})[1 + s\boldsymbol{C}_{\mathrm{eq}}^{\mathrm{p}}/\boldsymbol{G}_{\mathrm{eq}}^{\mathrm{p}} + 1/(s\boldsymbol{L}_z\boldsymbol{G}_{\mathrm{eq}}^{\mathrm{p}})]$, $\boldsymbol{B}_f = \boldsymbol{G}_{\mathrm{eq}}^{\mathrm{p}}$, $\boldsymbol{D}_f = \boldsymbol{R}_{\mathrm{eq}} + s\boldsymbol{L}_{\mathrm{eq}}$.

According to (1) and (3), the terminal voltage difference before and during the fault is

$$\Delta\boldsymbol{U}(s) = \boldsymbol{A}_f\Delta_{\boldsymbol{B}}\boldsymbol{U}(s) + \Delta_{\boldsymbol{A}}\boldsymbol{B}\boldsymbol{U} - \Delta_{\boldsymbol{D}}\boldsymbol{I}_k^{\mathrm{p}}(s) \tag{5}$$

where $\Delta_{\boldsymbol{A}} = \boldsymbol{A}_f - \boldsymbol{A}$, $\Delta_{\boldsymbol{B}} = \boldsymbol{B}_f - \boldsymbol{B}$; $\Delta_{\boldsymbol{D}} = \boldsymbol{D}_f - \boldsymbol{D}$.

Set the tuning parameters ψ and the auxiliary voltage signal Υ, the terminal voltage with auxiliary signals is

$$\widetilde{\boldsymbol{U}}_{kf}^{\mathrm{q}}(s) = \Delta\boldsymbol{U}(s) + \boldsymbol{U}_k^{\mathrm{q}}(s) + \boldsymbol{A}_f(\boldsymbol{B}_f - \boldsymbol{B})\psi\Upsilon \tag{6}$$

The terminal voltage during the fault is

$$\widetilde{\boldsymbol{U}}_{kf}^{\mathrm{q}}(s) = \boldsymbol{A}_f\left[\boldsymbol{B}_f\boldsymbol{B}\right]\begin{bmatrix}\boldsymbol{U}(s) + \psi\Upsilon\\ -\psi\Upsilon\end{bmatrix} - \boldsymbol{D}_f\boldsymbol{I}_k^{\mathrm{p}}(s) \tag{7}$$

Obviously, the fault scaling factor $d = 0$ and $\boldsymbol{R}_f$ is infinite when the system is normal states, then equation (7) is

$$\begin{aligned}\widetilde{\boldsymbol{U}}_{kf}^{\mathrm{q}}(s) &= \boldsymbol{A}_f\left[\boldsymbol{B}_f\boldsymbol{B}\right]\begin{bmatrix}\boldsymbol{U}(s) + \psi\Upsilon\\ -\psi\Upsilon\end{bmatrix} - \boldsymbol{D}_f\boldsymbol{I}_k^{\mathrm{p}}(s)\\ &= \boldsymbol{A}\boldsymbol{B}\boldsymbol{U}(s) - \boldsymbol{D}\boldsymbol{I}_k^{\mathrm{p}}(s) = \boldsymbol{U}_k^{\mathrm{q}}(s)\end{aligned} \tag{8}$$

In other words, the injected auxiliary voltage signal has no impact on the terminal voltage of the line when the system is operating normally.

B. FAULT DETECTION METHOD

1) DATA RECONSTRUCTION

Due to the inconsistency of fault manifestations at different scales [26], measured data are reconstructed by scale-level signal energy entropy ratio for highlighting the fault feature.

Compared with wavelet transform, VMD has adaptive decomposition ability, high decomposition stability, and can reflect signal transient characteristics well [27]. Therefore, VMD decomposes the measured voltage data into K IMFs in this section.

$$\begin{cases}\lim\limits_{\{u_k\},\{\omega_k\}}\left\{\sum\limits_{k=1}^{\mathrm{K}}\left\|\,\partial_t\left[\left(\delta(t) + \dfrac{j}{\pi\,t}\right) * \boldsymbol{u}_k(t)\right]\mathrm{e}^{-j\omega_k t}\,\right\|_2^2\right\}\\ \text{s.t.}\ \sum\limits_{k=1}^{\mathrm{K}}\boldsymbol{u}_k = \widetilde{\boldsymbol{u}}\end{cases} \tag{9}$$

Then, the energy sequence of the $k-$th IMF is obtained by the teager energy operator [28]

$$E_k(n) = u_k^2(n) - u_k(n+1)u_k(n-1) \tag{10}$$

Furthermore, the energy entropy of the $k-$th IMF is

$$\Re_k(i) = -\sum_{n=(i-1)\phi+1}^{i\phi}\kappa_k(n)\log_2\kappa_k(n) \tag{11}$$

The weight of the $k-$th mode in the $i-$th window is

$$\delta_k^i = \frac{\widehat{\Re}_k(i)}{\overline{\Re}_k(i)} \tag{12}$$

Then, the reconstructed $k-$th IMF $\widehat{\boldsymbol{u}}_k$ is

$$\widehat{\boldsymbol{u}}_k = \left(\boldsymbol{u}_k^i\delta_k^i\right)_{1\times N} \tag{13}$$

Thereby, the data reconstructed $\boldsymbol{u}$ is

$$\boldsymbol{u} = \sum_{k=1}^{\mathrm{K}}\widehat{\boldsymbol{u}}_k \tag{14}$$

2) FAULT DETECTION METHOD

Due to the significant differences in the probability distribution of voltage signals before and during the fault [19], this paper uses statistical divergence for fault detection.

Let $\overline{\boldsymbol{u}}$ and $\widehat{\boldsymbol{u}}$ be the reconstructed normal data and measured data, respectively. Suppose $\overline{\boldsymbol{u}}$ and $\widehat{\boldsymbol{u}}$ satisfy the probability distributions $\overline{\boldsymbol{P}}$ and $\widehat{\boldsymbol{P}}$, that is, $\overline{\boldsymbol{u}} \sim \overline{\boldsymbol{P}}$ and $\widehat{\boldsymbol{u}} \sim \widehat{\boldsymbol{P}}$. The Wasserstein divergence [29] between $\overline{\boldsymbol{P}}$ and $\widehat{\boldsymbol{P}}$ can be expressed as:

$$W_2\left(\overline{\boldsymbol{P}}, \widehat{\boldsymbol{P}}\right) = \left(\inf_{\pi\in\prod\left(\overline{\boldsymbol{P}},\widehat{\boldsymbol{P}}\right)}\int D(\overline{\boldsymbol{u}}, \widehat{\boldsymbol{u}})^2 d\pi\left(\overline{\boldsymbol{P}}, \widehat{\boldsymbol{P}}\right)\right)^{\frac{1}{2}} \tag{15}$$

where $\Pi\left(\overline{\boldsymbol{P}}, \widehat{\boldsymbol{P}}\right)$ represents the set of all joint probability distributions with edges $\overline{\boldsymbol{P}}$ and $\widehat{\boldsymbol{P}}$. $D(\overline{\boldsymbol{u}}, \widehat{\boldsymbol{u}})$ is the distance of the sample. The detection threshold is

$$\xi = \mu + \tau\sigma \tag{16}$$

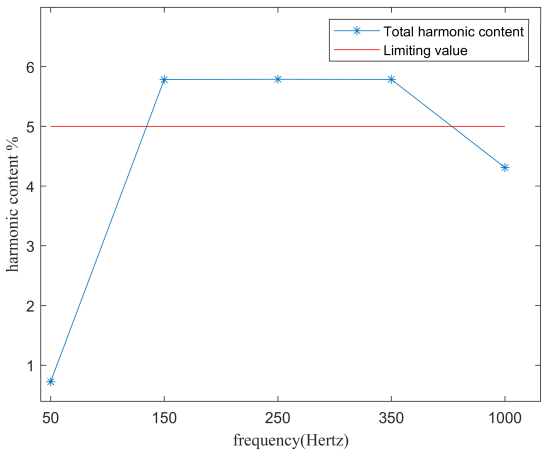

FIGURE 4. Total harmonic content.

Because of the high-impedance fault often lasts more than 8 cycles [30], the criteria for determination are:

$$\begin{cases} W_2 > \xi \\ t_{\mathrm{d}} > t_{\mathrm{w}} \end{cases} \tag{17}$$

When the power frequency of the system is 50 Hz, set t_{w} to 160 ms.

III. AUXILIARY SIGNAL SELECTION PRINCIPLE

A. AMPLITUDE SELECTION PRINCIPLE

In the distribution network, the accuracy of voltage transformers is generally not less than 3% of the rated value [31]. Therefore, in order to ensure accuracy, the amplitude of the auxiliary signal should not be less than the maximum detection accuracy of the transformer. Moreover, in order to avoid injecting auxiliary signals and distorting the voltage amplitude too high [18], the auxiliary signal should be below 15%.

B. FREQUENCY SELECTION PRINCIPLE

According to IEEE standards [32], the single harmonic content and total harmonic content for 1 kV - 69 kV common connection points cannot exceed 3% and 5%, respectively. Because 50 Hz, 150 Hz, 250 Hz, 350 Hz, and 1000 Hz have been used in relevant research results [33], [34], [35], this paper analyzes the harmonic distortion rate of these frequencies in the 10kV power grid. The result is shown in Figure 4.

However, the 7th harmonic content of the 1000 Hz signal is 4.28%, exceeding the limit, only the 50 Hz signals meet the IEEE standard.

IV. SIMULATION VERIFICATION

In this paper, PSCAD/EMTDC is used to build an improved IEEE 34 node system, as shown in Figure 5. The auxiliary signal is injected at the 806th node.

The high-impedance fault model used was proposed by Emanue et al [36] used is shown in Figure 6.

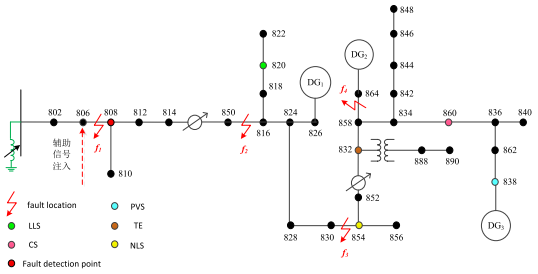

FIGURE 5. Improved IEEE 34 node system.

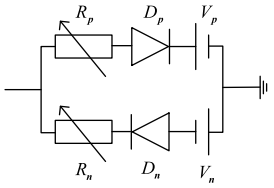

FIGURE 6. Structure diagram of high-impedance fault model.

TABLE 2. High-impedance fault model parameters.

Parameter	R_N/R_P(kΩ)	V_p(kV)	V_n(kV)
Numerical value	15-75	1.2-4.5	1.4-4.2

The high-impedance fault parameters used in this study are presented in Table 2.

Fault detection performance is evaluated for transition impedances of 15 kΩ − 75 kΩ for an A-phase earthing fault. The measurement noise is considered to follow a Gaussian distribution. The high impedance fault occurs at 0.5 s for a duration of 0.5 s. The VMD penalty factor is set to 4000, and the number of decomposed modes is 4 in all scenarios. In this paper, four scenarios are set to test the proposed method performance as follows:

S_1: The fault happened at Line 806-808 with 1796.559 m away from the 806th node.

S_2: The fault happened at Line 850-816 with 28.799 m away from the 850th node.

S_3: The fault happened at Line 830-854 with 24.154 m away from the 830th node.

S_4: The fault happened at Line 858-864 with 37.625 m away from the 858th node.

All photovoltaic power sources are put into operation for four scenarios. A phase-locked loop and a limiting device are applied to obtain an auxiliary signal, the same frequency and phase as the power frequency voltage, and the amplitude of the auxiliary signal is 5% of the peak value of the normal voltage.

A. THE INFLUENCE OF AUXILIARY SIGNAL INJECTED

To verify the impact of auxiliary signal injection on the measured signal during the fault period. A HIF happened

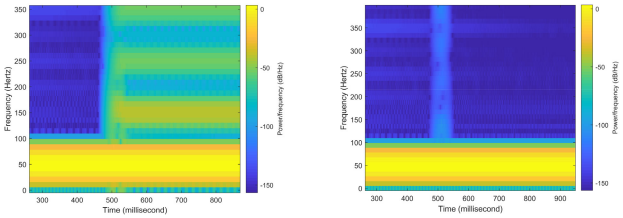

(a) Spectrum diagram with AFFE (b) Spectrum without AFFE

FIGURE 7. Voltage spectrum diagram.

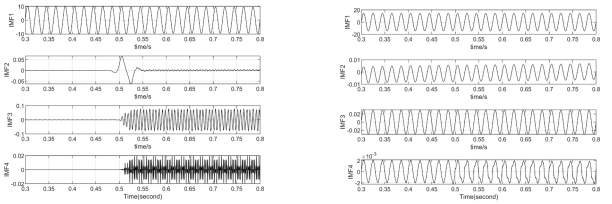

(a) Spectrum diagram with AFFE (b) Spectrum without AFFE

FIGURE 8. Voltage decomposition results.

in scenario S_1 with transient resistance 35 kΩ. For voltage with/without AFFE, Figure 7 shows the frequency spectrum.

As shown in Figure 7, the spectrum characteristics with and without AFFE are mainly concentrated around 50 Hz, and there is a change at 500 ms, indicating that the fault occurred at 500 ms. Compared to the case without AFFE,the energy in each frequency band significantly increases in the case of AFFE after a fault occurs. Specifically, after a fault occurs, the energy above 100Hz significantly increases, especially around 150Hz where the energy increases the most. In addition, the energy of odd harmonics is higher than that of even harmonics. On the other hand, voltage signals without AFFE only show slight energy changes in the first 80ms after a fault occurs, there is no significant change in energy compared to normal in the following time period. Figure 8 shows the IMFs obtained by VMD.

As shown in Figure 8, it can be observed that the waveform of IMF1 is similar with and without AFFE. However, for IMF2-IMF4, in the presence of auxiliary signals, there is an apparent step-like phenomenon at the time of fault occurrence. On the contrary, no significant changes were observed in IMF2-IMF4 without AFFE.

B. FAULT DETECTION PERFORMANCE

This section validates the proposed method for fault scenarios with and without AFFE, considering aspects such as transient impedance, noise, fault location, and switching events.

1) DIFFERENT TRANSITION IMPEDANCES

To test the impact of transition impedance on detection results. When a fault occurs in scenario S_1, the impedance parameters of Table 2 are 15 kΩ, 35 kΩ, 55 kΩ, and 75 kΩ, respectively, the detection results with and without AFFE are shown in Figure 9.

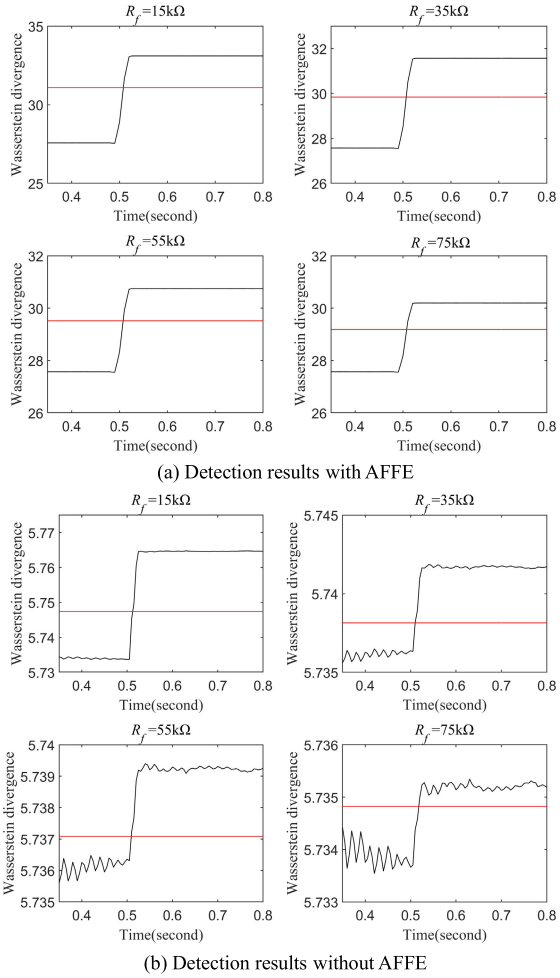

(a) Detection results with AFFE

(b) Detection results without AFFE

FIGURE 9. Detection results under different transition impedances.

As shown in Figure 9, corresponding to the transition impedances of 15 kΩ, 35 kΩ, 55 kΩ, and 75 kΩ, the detection curves with AFFE exceeded the limit at 3.6 ms, 3.66 ms, 3.82 ms, and 4.51 ms after the fault occurred, and remained above the threshold continuously. All detection results met the judgment conditions. The detection curves without AFFE exceeded the threshold at 9.98 ms, 10 ms, 10.13 ms, and 17.82 ms, respectively. Figure 8 shows that the detection curves with and without AFFE gradually decrease with the increase of transition impedance, and the amplitude of the detection curve exceeds the limit. However, from the detection results, it can meet the judgment conditions, but the detection curve without AFFE shows significant fluctuations.

2) DIFFERENT NOISE LEVELS

Due to the impact of noise on the detection results of high-impedance faults, in noise environments with signal to noise ratio of 30 dB, 25 dB, 20 dB, and 15 dB, when a fault occurs in scenario S_1, the impedance parameters of Table 2 is 75 kΩ, the detection results with and without AFFE are shown in Figure 10.

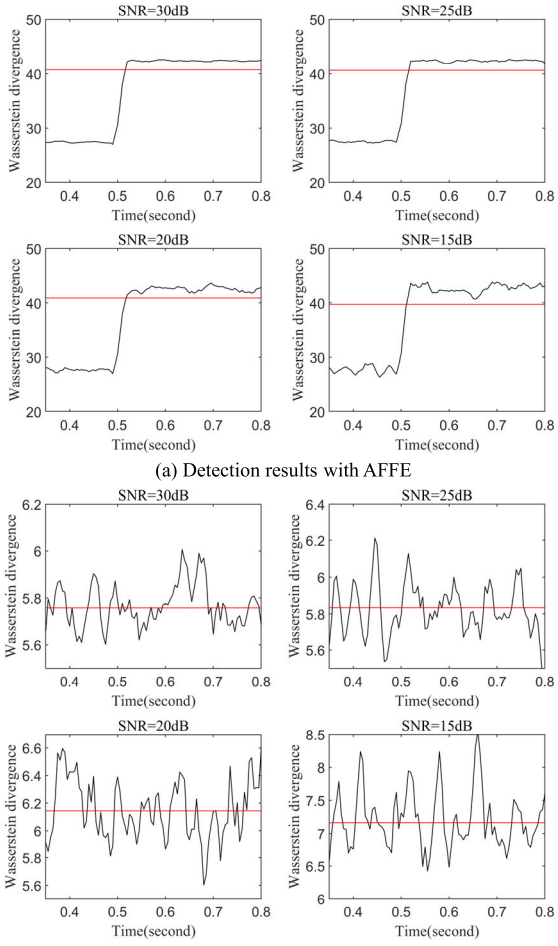

(a) Detection results with AFFE

(b) Detection results without AFFE

FIGURE 10. Detection results under different noises.

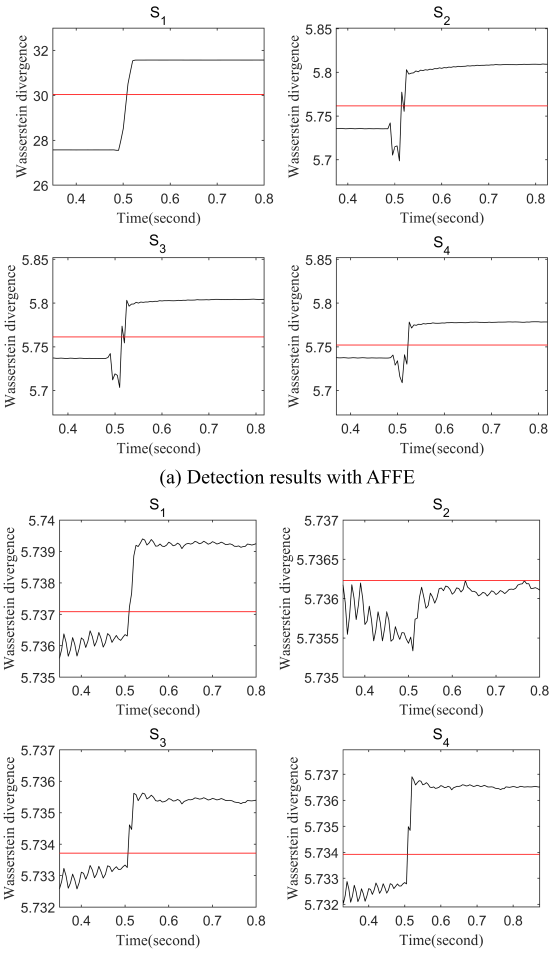

(a) Detection results with AFFE

(b) Detection results without AFFE

FIGURE 11. Detection results of different fault locations.

As shown in Figure 10, it can be seen that at 15.5 ms, 16.43 ms, 18.21 ms, and 19.28 ms after the fault occurred, the detection curves with AFFE corresponding to signal-to-noise ratios of 30 dB, 25 dB, 20 dB, and 15 dB, respectively exceeded the threshold and remained above the threshold, meeting the judgment criteria. The detection curve without AFFE will frequently exceed the threshold before and after the fault, and the continuous exceeding time does not meet the judgment conditions.

3) DIFFERENT FAULT LOCATIONS

In order to study the impact of different fault locations, when a fault occurs in scenarios S_1-S_4, the impedance parameters of Table 2 is 35 kΩ, the detection results with and without AFFE are shown in Figure 11.

As shown in Figure 11, corresponding to scenarios S_1, S_2, S_3, and S_4, the detection curves with AFFE exceeded the threshold at 3.66 ms, 7.08 ms, 7.2 ms, and 23.33 ms after the fault occurred, respectively, and remained above the threshold, meeting the fault determination conditions. The detection curves of scenarios S_1, S_3, and S_4 without AFFE exceeded the threshold at 9.24 ms, 16.75 ms, and 17.65 ms, respectively, and remained consistently above the threshold. The detection curve of scenario S_2 does not exceed the threshold, and the duration does not meet the judgment criteria.

4) SWITCHING EVENT

Switching events can generate transient characteristics similar to high-impedance faults. Therefore, this paper investigates the impact of different switching events on the proposed enhanced detection algorithm. The following five types of switching events are considered: LLS [37], NLS [38], CS [38], TE, and PVS [39]. The models for these five switching events are illustrated in Figure 12.

The locations of the switching events are shown in Figure 4. The parameters for switching scenarios are shown in Table 3.

a: LOAD SWITCHING EVENT

The detection results of switching scenarios 1 and 2 with and without AFFE are shown in Figures 13 and 14.

As shown in Figure 13, during LLS, the detection curves with AFFE exceeded the threshold twice at 0.4126 s and

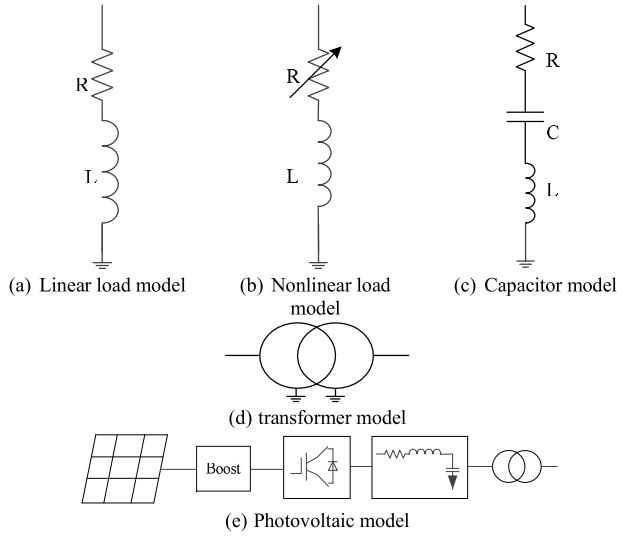

(a) Linear load model (b) Nonlinear load model (c) Capacitor model

(d) transformer model

(e) Photovoltaic model

FIGURE 12. Switching model.

TABLE 3. Switching scenarios.

Switching scenario	Switching type	access (s)	resection (s)	position	notes
1	LLS	0.4	0.7	820	0.5MW
2	NLS	0.4	0.7	854	0.5MW
3	CS	0.4	0.7	860	-
4	TE	0.7	0.4	832	-
5	PVS	0.7	0.4	835	1MW

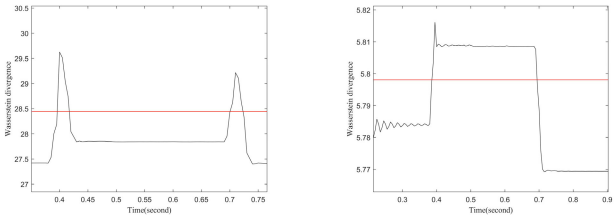

(a) Detection results with AFFE (b) Detection results without AFFE

FIGURE 13. LLS detection results.

0.7072 s, respectively, and were below the threshold at 0.4432 s and 0.7383 s, respectively. Continuously exceeding the threshold time does not meet the judgment criteria. The detection curve without AFFE exceeds the threshold in 0.38615s, until it drops below the threshold in 0.69415 s, and continues to exceed the threshold for 308 ms, meeting the judgment criteria. Figure 13 show that during LLS, the detection curve without AFFE may be misjudged as a fault.

As shown in Figure 14, during the NLS process, the detection curve with AFFE exceeded the threshold at 0.64252 s and dropped below the threshold at 0.7259 s. The process lasted for 83.38 ms, which did not meet the judgment criteria. The detection curves without AFFE exceeded the threshold at 0.4289 s and 0.51593 s, respectively, with a maximum duration of 185.87 ms, meeting the judgment criteria. Figure 14 show that during NLS, the detection curve without AFFE may be misjudged as a fault.

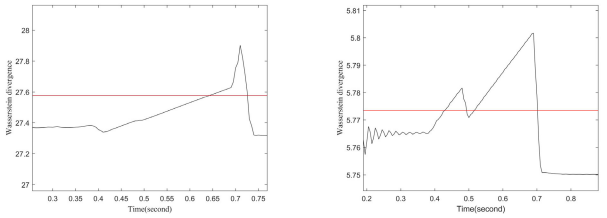

(a) Detection results with AFFE (b) Detection results without AFFE

FIGURE 14. NLS detection results.

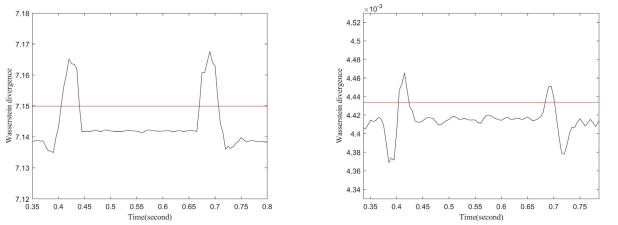

(a) Detection results with AFFE (b) Detection results without AFFE

FIGURE 15. CS detection results.

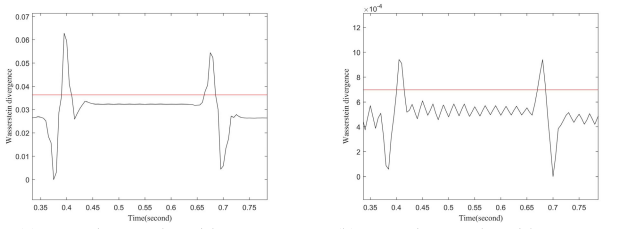

(a) Detection results with AFFE (b) Detection results without AFFE

FIGURE 16. TE detection results.

b: CAPACITOR SWITCHING AND TRANSFORMER ENERGIZATION EVENTS

The detection results with and without AFFE in switching scenarios 3 and 4 are shown in Figure 15 and Figure 16.

As shown in Figure 15, it can be seen that the detection curves with AFFE exceeded the threshold twice within 0.42501 s and 0.66980 s, respectively, and again fell below the threshold within 0.44017 s and 0.72674 s, with durations of 15.16 ms and 56.94 ms, respectively. In comparison, the detection curves without AFFE decreased at 0.38505 s and 0.72005 s, respectively, and exceeded the threshold twice at 0.40355 s and 0.68361 s, and dropped below the threshold at 0.42366s and 0.70131 s, respectively, with durations of 20.11 ms and 17.7 ms, respectively.

As shown in Figure 16, it can be seen that the detection curves with AFFE decrease at 0.37505 s and 0.69504 s, respectively. Afterward, they exceeded the threshold twice at 0.39016 s and 0.66344 s and again fell below the threshold at 0.40928 s and 0.68528 s, with durations of 19.12 ms and 21.84 ms, respectively. The detection curves without AFFE exceeded the threshold twice at 0.4004 s and 0.67013 s and then decreased to the threshold at 0.41485 s and 0.6858 s, with durations of 14.45 ms and 15.75 ms, respectively.

TABLE 4. Performance comparison.

Method	Mean time to detect (ms)	Maximum transition impedance (kΩ)	Reliability (%)	Safety (%)	Noise (dB)	Switching event
Proposed method with AFFE	6.18	75	98.33	100	15	LLS, NLS, CS, TE, PVS
Proposed method without AFFE	14.37	35	60.67	80	50	LLS, NLS, CS, TE, PVS
MM-DT [40]	30.66	12	98.77	100	-	LLS, NLS, CS
MM [41]	80	0.3	100	100	-	LLS, NLS, CS
SWT [42]	80	1	95.5	98.8	-	LLS, NLS, CS, TE
DFT-KF [43]	126	1.5	98.3	95.7	-	LLS

Notes: MM: Mathematical morphology, DT: Decision tree, SR: Stochastic resonance, SWT: stationary wavelet transform, DFT: Discrete Fourier transform, KF: Kalman filter, reliability: Total number of HIFs predicted/actual number of HIF cases, safety: Total number of non HIF forecasts/actual number of non HIF scenarios.

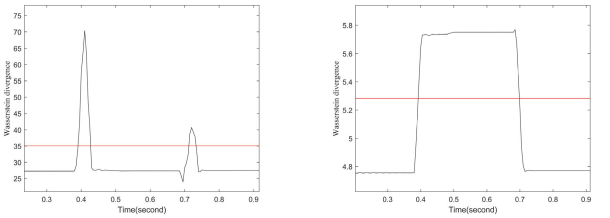

(a) Detection results with AFFE (b) Detection results without AFFE

FIGURE 17. PVS detection results.

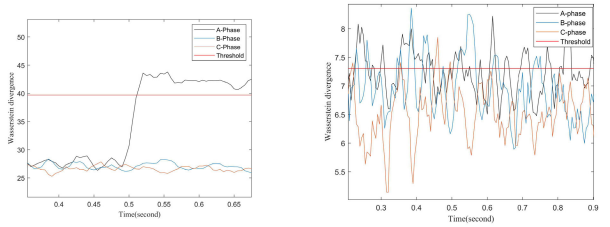

(a) Detection results with AFFE (b) Detection results without AFFE

FIGURE 18. Fault phase identification results.

c: PHOTOVOLTAIC SWITCH EVENT

The detection results of with and without AFFE in switching scenarios 5 are shown in Figure 17.

As shown in Figure 17, it can be seen that the detection curve with AFFE exceeded the threshold twice at 0.3906 s and 0.7121 s, respectively, and fell below the threshold again at 0.42729 s and 0.7331 s, with durations of 36.69 ms and 21 ms, respectively. The duration did not meet the judgment criteria. The detection curve without AFFE exceeds the threshold within 0.39248 s. However, the curve drops below the threshold at 0.69852 s and lasts 306.04 ms. The event may be misjudged as a fault occurrence.

C. FAULT PHASE IDENTIFICATION

When scenario S_1 experiences a phase a fault with an impedance parameter of 75 kΩ from Table2 in a 15 dB noise environment, the three-phase voltage detection results with and without AFFE are shown in Figure 18.

As shown in Figure 18, it can be seen that in the presence of AFFE, compared with the detection curve of phase A, the detection results of phase A, phase B, and phase C significantly increase after the fault occurs. 16.4 ms after the fault occurred, the A-phase detection result exceeded the threshold and remained above it, meeting the discrimination criteria. However, the measurement results of phase B and phase C never exceeded the threshold; In the absence of it can be seen that in the presence of AFFE, the measurement results of phase A, phase B, and phase C have been fluctuating within the upper and lower range of the threshold, and the maximum duration exceeding the threshold does not meet the judgment criteria.

D. PERFORMANCE COMPARISON

In order to validate the real-time capability, enhanced detection capability under higher transition impedance, and the impact on switching events, the proposed fault feature enhancement method is compared with existing fault detection methods from references [40], [41], [42], [43] The comparison results are presented in Table 4.

According to Table 4, the proposed fault feature enhancement method in this paper achieves an average fault detection time of 5.34 ms and can tolerate a maximum transition impedance of 75 kΩ under an SNR of 15 dB. Compared to the non-enhanced methods, MM-DT, MM, SWT, and DFT-KF detection algorithms, the proposed fault feature enhancement method exhibits significant superiority in terms of detection time and impedance to transition impedance, and can reliably detect faults under 15 dB noise.

V. EXPERIMENTAL TEST

A. CASE 1

A fault experiment was conducted on the A-phase cement surface in an actual 10kV distribution network. The fault occurred 500 meters away from the busbar, and the protection did not operate during the duration of the fault. The single-line diagram is shown in Figure 19, and the on-site grounding experimental device is shown in Figure 20.

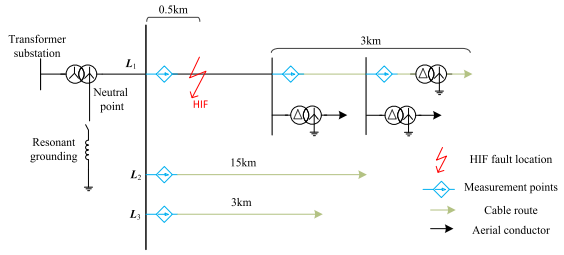

FIGURE 19. Actual 10kV distribution network single line diagram.

FIGURE 20. On site grounding experimental device.

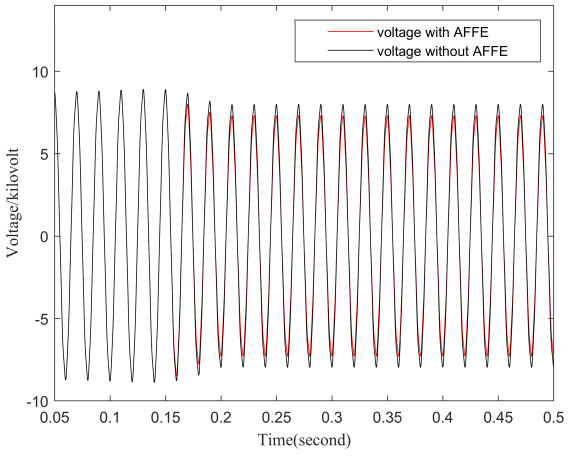

FIGURE 21. Field voltage waveform.

In the actual 10 kV distribution network, under the condition of resonant grounding of the neutral point, conduct fault experiments on the A-phase connected cement surface. The A-phase voltage waveforms with and without auxiliary signals based on experimental data are shown in Figure 21. Based on this work, further research will be conducted on the optimization selection of auxiliary signals, design of generation devices, injection methods, and other aspects.

As shown in Figure 21, the with AFFE leads to a decrease in voltage magnitude by approximately 4.7% compared to the without AFFE after the fault occurrence. The detection results of the three-phase voltages are shown in Figure 22.

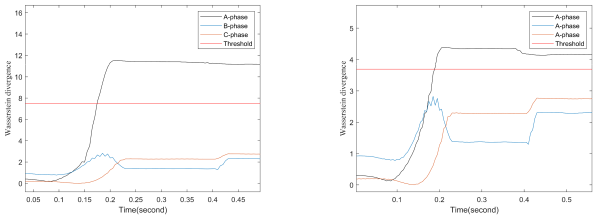

(a) Detection results with AFFE (b) Detection results without AFFE

FIGURE 22. Detection results.

(a) Damp grassland (b) Cement ground with damp surface

(c) Moist soil (d) Brick

FIGURE 23. On site experiments with different media.

As shown in Figure 22, regardless of whether there is AFFE, only the A-phase detection curve exceeds the threshold, while the detection curves of both B-phase and C-phase are below the threshold. The detection curve with AFFE exceeded the threshold at 14.35 ms after the fault and remains above the threshold. The detection curve without AFFE exceeded the threshold at 28.504 ms after the fault occurred but decreased at 0.38 s but did not fall below the threshold.

B. CASE 2

In the actual 10 kV distribution network, HIF experiments were conducted on the grounding medium of phase A, which was wet grassland, wet cement ground, wet soil, and bricks. The fault occurred at a distance of 4 km from the bus, during which the protection did not operate. The on-site experimental images and voltage waveforms of different grounding media are shown in Figure 23- Figure 24.

The detection results of A-phase voltage for damp grassland, cement ground with damp surface, moist soil, and brick grounding are shown in Figure 25- Figure 27.

As shown in Figure 25 - Figure 27, the detection curves with AFFE exceeded the threshold at 12.4 ms, 18.6 ms, 11.7 ms, and 14.6 ms after the fault with damp grass, damp cement, damp soil, and bricks, respectively. Although the detection curve of moist soil as the grounding medium showed a decrease, it remained above the threshold. However,

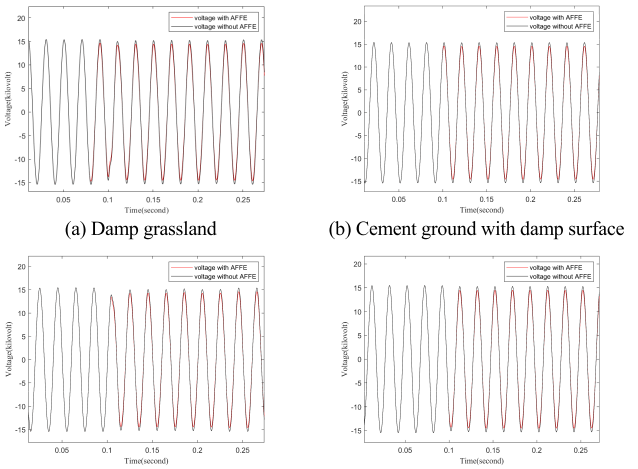

(a) Damp grassland (b) Cement ground with damp surface

(c) Moist soil (d) Brick

FIGURE 24. Fault voltage recording of different grounding media.

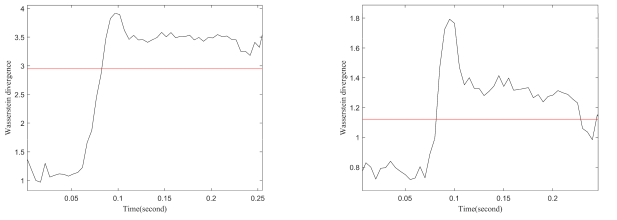

(a) Detection results with AFFE (b) Detection results without AFFE

FIGURE 25. Grounding test results for damp grassland.

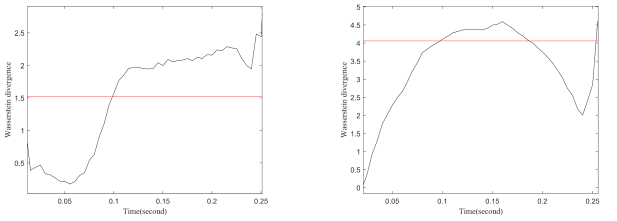

(a) Detection results with AFFE (b) Detection results without AFFE

FIGURE 26. Grounding test results of cement ground with damp surface.

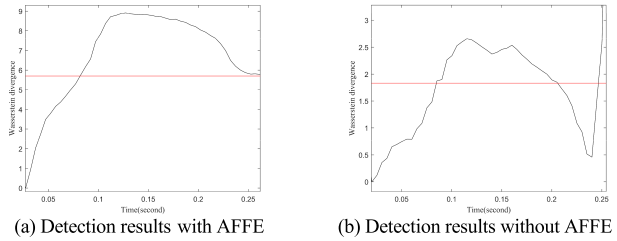

(a) Detection results with AFFE (b) Detection results without AFFE

FIGURE 27. Grounding test results for moist soil.

detection curves without AFFE exceeded the threshold at 11.4 ms, 17.5 ms, 14.6 ms, and 12.8 ms after the fault, respectively. Then, the detection curves dropped at the thresholds of 0.2283 s, 0.1869 s, 0.2058 s, and 0.1638 s, respectively. That is, the detection curves without AFFE sustain 15.9 ms, 66.6 ms, 40.7 ms, and 89.7 ms above the threshold,

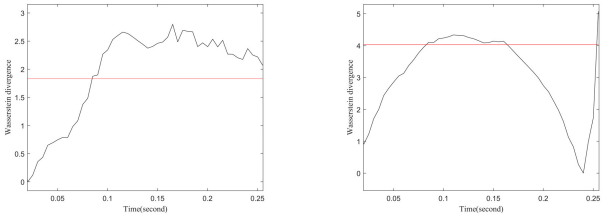

(a) Detection results with AFFE (b) Detection results without AFFE

FIGURE 28. Grounding test results for brick.

respectively. The detection results without AFFE lead to false discriminations (no faults happened) according to the criteria.

VI. CONCLUSION

In this paper, an active high-impedance fault detection method is proposed in resonant grounding distribution networks. Firstly, analyze the voltage difference at the end of the line before and after the fault, and inject auxiliary signals of appropriate frequency and amplitude into the starting point of the line. Enhance the terminal voltage of the line during faults without affecting normal operation. Then, by utilizing the energy difference at the local scale before and after the fault, the signal is reconstructed to further highlight the fault characteristics. Finally, use Wasserstein divergence to detect HIF.

The proposed method was validated and compared using simulation and experimental data. Different fault scenarios and switching events, such as transition impedances, fault locations, noise, and LLS, NLS, CS, TE, and PVS, were simulated. The simulation results indicate that AFFE does not affect the voltage at the end of the line during normal operation. When a fault occurs, it enhances the fault characteristics. In addition, the proposed detection method is robust to transition impedance, fault localization, and noise. This method can detect HIF of 75 kΩ in a noisy environment with a signal-to-noise ratio of 15 dB, and the switching event does not affect the detection performance. Under the same detection method, compared to the detection results without AFFE, the detection results with AFFE increased the transition impedance by 40 kΩ, improved reliability and safety by 37.66% and 20%, respectively, and advanced the average detection time by 8.19ms. It indicates that AFFE can significantly improve the algorithm's sensitivity to HIF with large grounding impedances and improve the reliability and safety of the detection method. Compared with other detection methods, the method proposed in this paper has good robustness to transition impedance and noise.

Based on this work, further research will be conducted on the following aspects: Auxiliary signal optimization selection. Utilize existing modular multilevel converters, new energy equipment, or self-designed equipment in the distribution network to generate the designed auxiliary signal.

REFERENCES

[1] M. Mitolo, R. Musca, M. Tartaglia, and G. Zizzo, "Electrical safety analysis in the presence of resonant grounding neutral," *IEEE Trans. Ind. Appl.*, vol. 55, no. 5, pp. 4483–4489, Sep. 2019.

[2] M. Wei, F. Shi, H. Zhang, and W. Chen, "Wideband synchronous measurement-based detection and location of high impedance fault for resonant distribution systems with integration of DERs," *IEEE Trans. Smart Grid*, vol. 14, no. 2, pp. 1117–1134, Mar. 2023.

[3] L. G. de Oliveira, M. D. L. Filomeno, L. F. Colla, H. V. Poor, and M. V. Ribeiro, "Analysis of typical PLC pulses for sensing high-impedance faults based on time-domain reflectometry," *Int. J. Electr. Power Energy Syst.*, vol. 135, Feb. 2022, Art. no. 107168.

[4] É. M. Lima, R. D. A. Coelho, N. S. D. Brito, and B. A. D. Souza, "High impedance fault detection method for distribution networks under non-linear conditions," *Int. J. Electr. Power Energy Syst.*, vol. 131, Oct. 2021, Art. no. 107041.

[5] A. Mohammadi, M. Jannati, and M. Shams, "A protection scheme based on conditional generative adversarial network and convolutional classifier for high impedance fault detection in distribution networks," *Electr. Power Syst. Res.*, vol. 212, Nov. 2022, Art. no. 108633.

[6] F. Mumtaz, M. Asif, and H. H. Khan, "High impedance faults detection and classification in renewable energy-based distribution networks using time-varying Kalman filtering technique," *Eng. Proc.*, vol. 20, no. 1, pp. 1–6, Aug. 2022.

[7] M. Biswal, S. Ghore, O. P. Malik, and R. C. Bansal, "Development of time-frequency based approach to detect high impedance fault in an inverter interfaced distribution system," *IEEE Trans. Power Del.*, vol. 36, no. 6, pp. 3825–3833, Dec. 2021.

[8] M. Y. Suliman and M. T. Alkhayyat, "High impedance fault detection in radial distribution network using discrete wavelet transform technique," *Arch. Electr. Eng.*, vol. 70, no. 4, pp. 873–886, Jan. 2021.

[9] J. Yuan, Y. Hu, and Z. Jiao, "Faulty feeder detection method for SLG faults in distribution networks based on comprehensive fault characteristics across entire frequency spectrum," *Int. J. Electr. Power Energy Syst.*, vol. 140, Sep. 2022, Art. no. 107835.

[10] Z. Zhang, J. Ren, X. Tang, S. Jing, and W.-J. Lee, "Novel approach for arc fault identification with transient and steady state based time-frequency analysis," *IEEE Trans. Ind. Appl.*, vol. 58, no. 4, pp. 4359–4369, Jul. 2022.

[11] M. Biswal, C. Durga Prasad, P. Ray, and N. Kishor, "Modified complete ensemble empirical mode decomposition based HIF detection approach for microgrid system," *Int. J. Electr. Power Energy Syst.*, vol. 141, Oct. 2022, Art. no. 108254.

[12] N. Narasimhulu, D. V. A. Kumar, and M. V. Kumar, "LWT based ANN with ant lion optimizer for detection and classification of high impedance faults in distribution system," *J. Electr. Eng. Technol.*, vol. 15, no. 4, pp. 1631–1650, May 2020.

[13] V. Veerasamy, N. I. A. Wahab, M. L. Othman, S. Padmanaban, K. Sekar, R. Ramachandran, H. Hizam, A. Vinayagam, and M. Z. Islam, "LSTM recurrent neural network classifier for high impedance fault detection in solar PV integrated power system," *IEEE Access*, vol. 9, pp. 32672–32687, 2021.

[14] H. Teimourzadeh, A. Moradzadeh, M. Shoaran, B. Mohammadi-Ivatloo, and R. Razzaghi, "High impedance single-phase faults diagnosis in transmission lines via deep reinforcement learning of transfer functions," *IEEE Access*, vol. 9, pp. 15796–15809, 2021.

[15] M. Sarwar, F. Mehmood, M. Abid, A. Q. Khan, S. T. Gul, and A. S. Khan, "High impedance fault detection and isolation in power distribution networks using support vector machines," *J. King Saud Univ.-Eng. Sci.*, vol. 32, no. 8, pp. 524–535, Dec. 2020.

[16] Y. Zhang, X. Wang, J. He, Y. Xu, F. Zhang, and Y. Luo, "A transfer learning-based high impedance fault detection method under a cloud-edge collaboration framework," *IEEE Access*, vol. 8, pp. 165099–165110, 2020.

[17] H. Liu, S. Liu, J. Zhao, T. Bi, and X. Yu, "Dual-channel convolutional network-based fault cause identification for active distribution system using realistic waveform measurements," *IEEE Trans. Smart Grid*, vol. 13, no. 6, pp. 4899–4908, Nov. 2022.

[18] S. Nezamzadeh-Ejieh and I. Sadeghkhani, "HIF detection in distribution networks based on Kullback–Leibler divergence," *IET Gener., Transmiss. Distrib.*, vol. 14, no. 1, pp. 29–36, Jan. 2020.

[19] Y. Liu, Y. Zhao, L. Wang, C. Fang, B. Xie, and L. Cui, "High-impedance fault detection method based on feature extraction and synchronous data divergence discrimination in distribution networks," *J. Mod. Power Syst. Clean Energy*, vol. 11, no. 4, pp. 1235–1246, Jul. 2023.

[20] X. Xiong, J. Hongkai, X. Li, and M. Niu, "A Wasserstein gradient-penalty generative adversarial network with deep auto-encoder for bearing intelligent fault diagnosis," *Meas. Sci. Technol.*, vol. 31, no. 4, Jan. 2020, Art. no. 045006.

[21] L. Cui, Y. Liu, L. Wang, J. Chen, and X. Zhang, "High-impedance fault detection method based on sparse data divergence discrimination in distribution networks," *Electr. Power Syst. Res.*, vol. 223, Oct. 2023, Art. no. 109514.

[22] R. Xu, G. Song, Z. Chang, C. Zhang, J. Yang, and X. Yang, "A ground fault section location method based on active detection approach for non-effectively grounded DC distribution networks," *Int. J. Electr. Power Energy Syst.*, vol. 152, Oct. 2023, Art. no. 109174.

[23] G. Song, J. Hou, and B. Guo, "Single-ended fault location of hybrid MMC-HVDC system based on active detection," *Power Syst. Technol.*, vol. 45, no. 2, pp. 730–740, Jan. 2021.

[24] T. Bi, S. Wang, and K. Jia, "Single pole-to-ground fault location method for MMC-HVDC system using active pulse," *IET Gener., Transmiss. Distrib.*, vol. 12, no. 2, pp. 272–278, Jan. 2018.

[25] J.-Y. Wu, S. Lan, S.-J. Xiao, and Y.-B. Yuan, "Single pole-to-ground fault location system for MMC-HVDC transmission lines based on active pulse and CEEMDAN," *IEEE Access*, vol. 9, pp. 42226–42235, 2021.

[26] X. Wang, J. Gao, X. Wei, G. Song, L. Wu, J. Liu, Z. Zeng, and M. Kheshti, "High impedance fault detection method based on variational mode decomposition and Teager–Kaiser energy operators for distribution network," *IEEE Trans. Smart Grid*, vol. 10, no. 6, pp. 6041–6054, Nov. 2019.

[27] N. K. Sharma, S. R. Samantaray, and C. N. Bhende, "VMD-enabled current-based fast fault detection scheme for DC microgrid," *IEEE Syst. J.*, vol. 16, no. 1, pp. 933–944, Mar. 2022.

[28] I. Kamwa, A. K. Pradhan, and G. Joós, "Robust detection and analysis of power system oscillations using the Teager–Kaiser energy operator," *IEEE Trans. Power Syst.*, vol. 26, no. 1, pp. 323–333, Feb. 2011.

[29] L. Cui and Y. Liu, "High impedance fault detection method based on data divergence in the distribution network," in *Proc. IEEE Power Energy Soc. Gen. Meeting (PESGM)*, Jul. 2022, pp. 1–6.

[30] B. K. Chaitanya, A. Yadav, and M. Pazoki, "An intelligent detection of high-impedance faults for distribution lines integrated with distributed generators," *IEEE Syst. J.*, vol. 14, no. 1, pp. 870–879, Mar. 2020.

[31] *IEEE Recommended Practice for the Application of Instrument Transformers in Industrial and Commercial Power Systems*, IEEE Standard 3004.1, 2013.

[32] *IEEE Recommended Practice and Requirements for Harmonic Control in Electric Power Systems*, IEEE Standard 519, 2014.

[33] M. Hamzeh, S. Farhangi, and B. Farhangi, "A new control method in PV grid connected inverters for anti-islanding protection by impedance monitoring," in *Proc. 11th Workshop Control Modeling Power Electron.*, Zurich, Switzerland, Aug. 2008, pp. 1–5.

[34] M. T. Chau and V. B. Chau, "Comprehensive analysis of the control strategy for hybrid active power filter with injection circuit," *Int. J. Sci. Eng. Technol.*, vol. 2, no. 7, pp. 694–699, Jul. 2013.

[35] J. Shiming, H. Cong, and H. Tongcheng, "Research on an underground electricity cable path detection system," in *Proc. 7th Int. Conf. Intell. Comput. Technol. Autom.*, Changsha, China, Oct. 2014, pp. 500–504.

[36] N. Elkalashy, M. Lehtonen, H. Darwish, M. Izzularab, and A.-M. Taalab, "Modeling and experimental verification of high impedance arcing fault in medium voltage networks," *IEEE Trans. Dielectr. Electr. Insul.*, vol. 14, no. 2, pp. 375–383, Apr. 2007.

[37] X. Wang, G. Song, J. Gao, X. Wei, Y. Wei, K. Mostafa, Z. Hu, and Z. Zhang, "High impedance fault detection method based on improved complete ensemble empirical mode decomposition for DC distribution network," *Int. J. Electr. Power Energy Syst.*, vol. 107, pp. 538–556, May 2019.

[38] W. C. Santos, F. V. Lopes, N. S. D. Brito, and B. A. Souza, "High-impedance fault identification on distribution networks," *IEEE Trans. Power Del.*, vol. 32, no. 1, pp. 23–32, Feb. 2017.

[39] A. Kalbat, "PSCAD simulation of grid-tied photovoltaic systems and total harmonic distortion analysis," in *Proc. 3rd Int. Conf. Electr. Power Energy Convers. Syst.*, Oct. 2013, pp. 1–6.

[40] K. Sekar and N. K. Mohanty, "Data mining-based high impedance fault detection using mathematical morphology," *Comput. Electr. Eng.*, vol. 69, pp. 129–141, Jul. 2018.

[41] S. Kavaskar and N. K. Mohanty, "Detection of high-impedance fault in distribution networks," *Ain Shams Eng. J.*, vol. 10, no. 1, pp. 5–13, Mar. 2019.

[42] S. H. Mortazavi, Z. Moravej, and S. M. Shahrtash, "A hybrid method for arcing faults detection in large distribution networks," *Int. J. Electr. Power Energy Syst.*, vol. 94, pp. 141–150, Jan. 2018.

[43] Q. Cui, K. El-Arroudi, and Y. Weng, "A feature selection method for high impedance fault detection," *IEEE Trans. Power Del.*, vol. 34, no. 3, pp. 1203–1215, Jun. 2019.

ZHIWEI YAO received the B.E. degree in smart grid information engineering from the Shandong University of Technology, Zibo, China, in 2021, where he is currently pursuing the M.E. degree with the School of Electrical and Electronic Engineering. His research interest includes active fault detection in distribution networks.

YANG LIU (Member, IEEE) received the Ph.D. degree from Tianjin University, Tianjin, China, in 2016. He is currently an Associate Professor with the College of Electrical and Electronic Engineering, Shandong University of Technology, Zibo, Shandong. His work has addressed power system protection and control, situational awareness, and the integration of renewable resources.

JIAN CHEN is currently a Senior Engineer with the Zibo Metrology Technology Research Institute, Shandong. Her research interests include the verification and calibration of measuring instruments, such as DC resistors, AC and DC currents, voltages, and electrical energy.

JINPENG JI received the B.S. degree in smart grid information engineering from the Shandong University of Technology, Zibo, China, in 2021, where he is currently pursuing the M.S. degree with the School of Electrical and Electronic Engineering. His research interest includes the detection of false data injection attacks in smart grids.

MENGDI ZHANG received the B.E. degree in measurement and control technology and instrument from the Qilu University of Technology (Shandong Academy of Sciences), Jinan, China, in 2020. He is currently pursuing the M.E. degree with the School of Electrical and Electronic Engineering, Shandong University of Technology. His research interest includes monitoring the condition of energy storage systems.

YANYONG GONG received the B.E. degree in agricultural electrification from Shenyang Agricultural University, Shenyang, China, in 2022. He is currently pursuing the M.E. degree with the School of Electrical and Electronic Engineering, Shandong University of Technology. His research interest includes fault location in distribution networks.